



Article

Spatial Effects of Landscape Patterns of Urban Patches with Different Vegetation Fractions on Urban Thermal Environment

Yu Zhang ¹, Yuchen Wang ^{2,*} and Nan Ding ¹¹ School of Geography, Geomatics and Planning, Jiangsu Normal University, Xuzhou 221116, China² School of Management Science and Engineering, Xuzhou University of Technology, Xuzhou 221018, China

* Correspondence: wangyuchen@cumt.edu.cn

Abstract: The landscape patterns of urban green spaces have been proven to be important factors that affect urban thermal environments. However, the spatial effect of the landscape patterns of urban patches with different vegetation densities on land surface temperature (LST) has not been investigated in detail. In this study, the built-up area of Xuzhou City was taken as the study region, and the four phases of Landsat 8 images and their corresponding ground observations from 2014 to 2020 were selected as the basic data. Normalized spectral mixture analysis and an improved mono-window algorithm were used to invert the vegetation component fraction (VF) and LST maps of the study area, respectively, and the surface patches were classified into five levels according to the VF values, from low to high. Four landscape-level and five class-level metrics were then selected to represent the landscape characteristics of each VF-level patch. The tested values of 60 and 780 m were regarded as the best grain size and spatial extent, respectively, in the calculation of all landscape metrics of ALL VF-level patches (VFLM) using the moving-window method. The results of bivariate Moran's I for VFLM and LST showed the following: (1) for landscape-level metrics, only the Shannon diversity index and patch diversity have substantial negative spatial correlations with LST (with average |Moran's I| < 0.2), indicating that the types of VF levels and the number of patches exert weak negative effects on the thermal environment for a certain area; (2) for class-level metrics such as percentage of landscape, patch cohesion index, largest patch index, landscape shape index, and aggregation index, only the class-level metrics of sub-high VF (LV4) and extreme-high (LV5) VF levels patches have significant negative spatial correlations with LST (with high Moran's I value, and high-high and low-high distributions in local indications of spatial association cluster maps), indicating that only the patches of high VF levels can effectively alleviate LST and that patch proportion, natural connectivity degree, predominance degree, shape complexity, and aggregation degree are important landscape factors for regulating the thermal environment. Principal component analysis and multiple linear regression were applied to determine the impact weights of the class-level VFLMs of LV4 and LV5 patches on LST, which revealed the contributions of these landscape metrics to mitigating the urban heat island effect (UHI). These results signify the importance of and differences in the spatial patterns of various VF-level patches for UHI regulation; these patterns can provide new perspectives and references for urban green space planning and climate management.

Keywords: urban vegetation; urban heat island effect; landscape patterns; spatial correlation; Landsat 8



Citation: Zhang, Y.; Wang, Y.; Ding, N. Spatial Effects of Landscape Patterns of Urban Patches with Different Vegetation Fractions on Urban Thermal Environment. *Remote Sens.* **2022**, *14*, 5684. <https://doi.org/10.3390/rs14225684>

Academic Editors: Yuji Murayama and Ruci Wang

Received: 30 September 2022

Accepted: 5 November 2022

Published: 10 November 2022

Publisher's Note: MDPI stays neutral with regard to jurisdictional claims in published maps and institutional affiliations.



Copyright: © 2022 by the authors. Licensee MDPI, Basel, Switzerland. This article is an open access article distributed under the terms and conditions of the Creative Commons Attribution (CC BY) license (<https://creativecommons.org/licenses/by/4.0/>).

1. Introduction

In the process of urbanization, many natural surfaces are replaced by dense sidewalks, buildings, and other surfaces that absorb and retain heat; urbanization not only changes the ground thermal radiation characteristics but also generates a large amount of anthropogenic heat, resulting in a condition wherein the atmospheric and surface temperatures in urban areas are higher than those in the surrounding suburban natural and agricultural areas. This phenomenon is known as the urban heat island effect (UHI), which is also a form of

air pollution and a major cause of global warming. UHI expansion not only deteriorates regional thermal environments [1] but also leads to increased energy consumption, thermal risk, air pollution, and pollution-related mortality [2], which seriously reduce the quality of living environments for urban residents [3]. The urban thermal environment has become a research hotspot in the field of urban ecology, environment, and climate, and methods that can mitigate the risks and negative consequences of UHI are urgently needed.

The development of open green spaces, also known as “green infrastructure” and “green space cold islands” [4], has become a widely accepted strategy for mitigating UHI. Vegetation can reduce temperature and increase humidity by transpiration and shielding against long- and short-wave radiation [5,6]. As important parts of urban ecosystems, urban forests and greening can effectively improve urban substrates and play a major role in regulating the temperature and mitigating UHI [7]. Green spaces containing a large number of vegetation canopies can cool the atmosphere and air by creating a shading effect [8]. Interconnected shadow areas called “Shadeways” can pass through the city along infrastructure corridors and roads, provide relatively high natural and artificial shadows, and align cool areas with active travel spaces [9,10]. According to the vegetation species and environmental conditions in urban areas, shadow areas have a cooling effect of between 2.3 °C and 2.5 °C [11].

The cooling effect of green spaces on UHI can be analyzed by evaluating the statistical relationship between land surface temperature (LST) and regional landscape patterns or vegetation indices [12]. Some vegetation indices, such as the normalized difference vegetation index (NDVI) and fractional vegetation coverage (FVC), have been proven to exhibit negative correlations with LST [13,14]. Owing to urban land restrictions, it is impossible to mitigate UHI only by increasing urban vegetation. In addition to expanding the number and scale of urban forests (in a limited manner), maximizing the eco-efficiency of urban vegetation is a fundamental strategy to mitigate the thermal environment. Therefore, optimizing the landscape patterns of urban vegetation has become an effective option for alleviating UHI. Landscape patterns describe the landscape features of an ecosystem, such as its spatial arrangement and configuration. Spatial composition represents the proportions of all types of land cover within a certain spatial unit, whereas spatial configuration refers to their physical arrangement and distribution [15]. Spatial composition and configuration can be quantified using various landscape metrics that describe different spatial characteristics [3]. Some reports have described the coverage, patch characteristics, and spatial distribution of urban vegetation using landscape metrics and then discussed the relationship between urban vegetation and UHI. The results show that the size, shape, and spatial distribution of vegetation patches have a significant impact on urban thermal environments and that increasing the area and density of vegetation patches can effectively reduce LST [16,17]. However, most studies on the relationship between urban vegetation landscape patterns and UHI consider urban forests and open green spaces as a single type of vegetation, and few studies have considered the differences in the regulation effects of patches with different vegetation densities on UHI.

In this study, Landsat 8 and ground observation data were used to extract information on the urban vegetation component fraction (VF) and LST, respectively, and the urban surface considered was divided into patches with different vegetation densities according to VF values. The LST and landscape metrics of these patches extracted using the moving-window method were then analyzed via geospatial and statistical approaches. The results revealed the spatial effect of the landscape pattern of urban patches with different VFs on the urban thermal environment. The detailed technical process was shown in Figure 1.

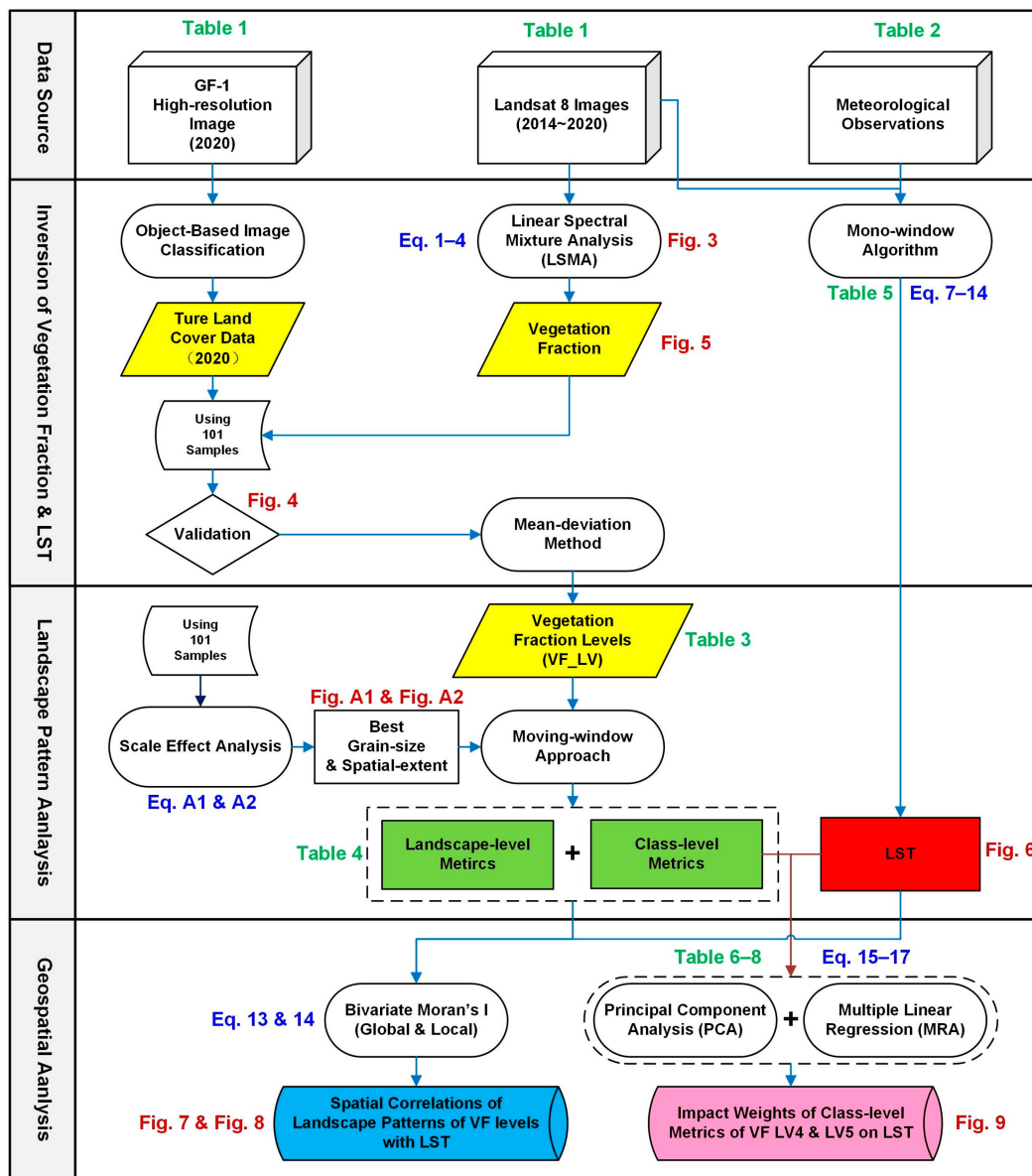


Figure 1. Technical roadmap of this study.

2. Materials and Methods

2.1. Study Area

The built-up area of Xuzhou, Jiangsu Province, was selected as the study location (Figure 2). Xuzhou is located southeast of the North China Plain (between 116°22′–118°40′E and 33°43′–34°58′N) and has a temperate monsoon climate. Xuzhou is an important transportation hub, an important coal-producing area in China, and an electric power base in eastern China. Xuzhou also has a large-scale manufacturing industry. However, the vegetation coverage rate of Xuzhou is as high as 32%, of which the urban vegetation coverage rate is 27.8%, making this city rank first in Jiangsu Province. The developed transportation and energy sectors, industries, and a large area of impervious surfaces have caused the built-up areas of Xuzhou to experience significant UHI. Simultaneously, the large area of urban vegetation has also played an important role in regulating the urban thermal environment. These characteristics of the study area make it suitable for exploring the spatial relationship between landscape patterns of patches with different vegetation densities and the urban thermal environment.

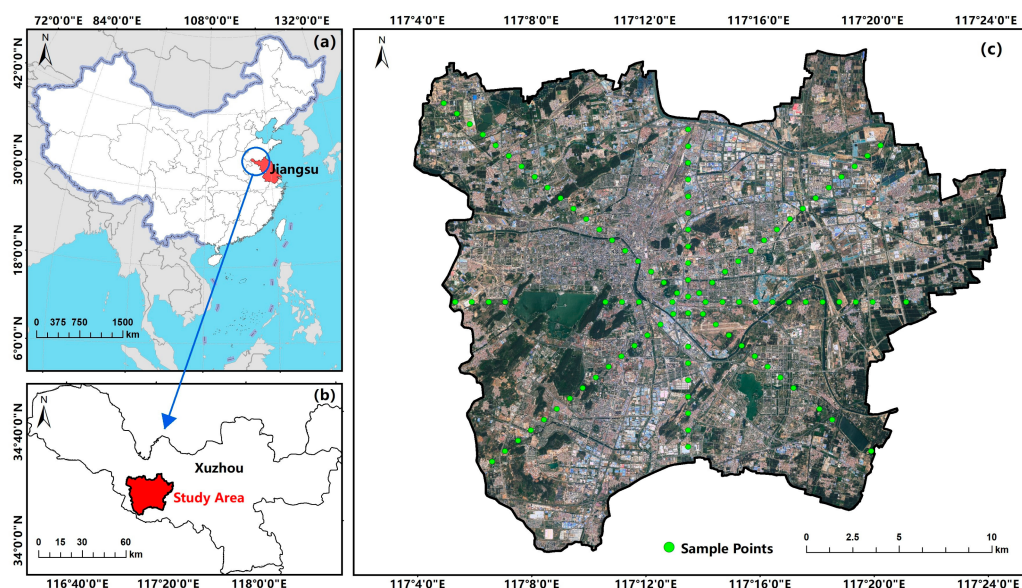


Figure 2. Location and satellite image of the study area. (a) Map of Jiangsu Province in China; (b) map of the study area in Xuzhou; and (c) GF-1 satellite image of the study area on 28 April 2020.

As shown in Figure 2c, a total of 101 sample points were selected in the study for the scale effect analysis and pixel unmixing validation in subsequent sections. At an interval of 900 m, the sample points were distributed on four sample lines from the city center to the suburb along four directions (east–west, south–north, southeast–northwest, and southwest–northeast). This distribution mode provides stable variation in the vegetation component ratio of the pixels along each sample line, owing to the sample pixels along each direction gradually changing from the suburb mainly covered by vegetation to the urban built-up area mainly covered by impervious surface, which ensures the diversity of the component ratios of the sample pixels.

2.2. Data Descriptions

2.2.1. Satellite Data

The remote sensing data used in this study included four Landsat 8 images from May 2014 to 2020 and one GF-1 image from April 2020. Detailed information is shown in Table 1. Visible and near-infrared bands 1–7 of the Landsat 8 OLI sensor were primarily used to extract mixed pixel endmember fractions and calculate other land surface parameters. Thermal infrared band 10 of the TIRS sensor was primarily used to invert LST. The spatial resolution of the fusion of the panchromatic and multispectral bands of the GF-1 image was 2 m; this resolution could be used to extract high-precision surface coverage data to verify the accuracy of the mixed pixel decomposition. As there are no high-resolution satellite data that completely coincide with the transit dates of the four phases of Landsat 8 images, the acquisition date of the GF-1 image used in this study was 28 April 2020, which is only 19 days from the acquisition date of the corresponding Landsat 8 image. Therefore, it is acceptable to use this GF-1 scene as the validation data.

2.2.2. Ground Observations

The necessary meteorological observations for the remote sensing inversion of LST included near-surface temperature and air relative humidity, as shown in Table 2. All the ground observations from 2014 to 2018 were obtained from the Collaborative Observation Test Site of the China University of Mining and Technology in the study area (data acquisition frequency: 30 min), and the meteorological data for 2020 were obtained from the NOAA National Centers for Environmental Information of USA [18] (data acquisition frequency: 1 h).

Table 1. Technical parameters of Landsat 8 and GF-1 data.

Satellite	Sensor Resolution	Scene ID	Acquisition Date	Acquisition Time (GMT + 8)
Landsat 8	OLI: 30 m TIRS: 100 m	LC81210362014121LGN00	1 May 2014	10:42:29
		LC81220362017136LGN00	16 May 2017	10:48:22
		LC81220362018123LGN00	3 May 2018	10:48:04
		LC81210362020138LGN00	17 May 2020	10:42:10
GF-1	PAN: 2 m MSS: 8 m	GF1_PMS1_E117.2_N34.1_20200428_L1A0004767917	28 April 2020	11:14:21
		GF1_PMS1_E117.3_N34.4_20200428_L1A0004767915	28 April 2020	11:14:17

Table 2. Ground meteorological observation data at satellite transit time.

Date	Acquisition Time (GMT + 8)	Air Temperature (K)	Air Relative Humidity (%)
1 May 2014	11:00:00	297.42	55.12
16 May 2017	11:00:00	296.33	39.76
3 May 2018	11:00:00	294.96	48.00
17 May 2020	11:00:00	299.48	53.19

2.3. Extraction of Vegetation Fraction from Mixed Pixels

2.3.1. Selection of Spectral Mixture Analysis Model

The pixels of low- and medium-resolution remote sensing images of urban areas are often mixed with endmembers, such as impervious surfaces, vegetation, and bare soil (water bodies generally exist independently). The commonly used methods for extracting the proportion of each endmember in a mixed pixel are divided into two categories: nonlinear and linear models. The theoretical premise of the linear spectral mixture analysis model (LSMA) is that the spectral signal of a pixel is a linear combination of the spectral signals of each endmember; the endmember fractions can be inverted using the least squares method based on the spectral characteristics of each endmember, simplifying the relationship between the components in the mixed pixel [19]. The fully constrained linear spectral mixture analysis model (FCLS), which is based on LSMA, adds two constraints: (1) the sum of all endmember fractions in each pixel is 100%; (2) all endmember fractions are non-negative [20]. The greater the number of endmembers, the more detailed the spectral analysis, which is beneficial to the fitting accuracy of FCLS. However, too many endmembers will increase the sensitivity of the decomposition results to endmember errors [21–23]. Based on a field investigation in the study area, the mixed pixel endmembers were divided into five types: forest, grassland (including grass, shrubs, and farmland), bare soil, and high- and low-albedo impervious surfaces (IPS). In addition, to solve the problems associated with brightness variation and shade, the reflectance values of all bands were normalized before applying FCLS [24]; the algorithms used were as follows.

$$\overline{R}_b = \frac{R_b}{\frac{1}{N} \sum_{b=1}^N R_b} \times 100 \quad (1)$$

$$\overline{R}_b = \sum_{i=1}^N f_i \overline{R}_{i,b} + e_b \quad (2)$$

$$\sum_{i=1}^N f_i = 1, \quad f_i \geq 0 \quad (3)$$

where \overline{R}_b is the normalized reflectance value of the mixed pixel for band b , R_b is the original reflectance of the mixed pixel for band b , N is the number of endmembers, f_i is the fraction of endmember i in the mixed pixel, $\overline{R}_{i,b}$ is the reflectance of endmember i for band b in the mixed pixel, and e_b is the model calculation residual for band b . The final fitting accuracy

of FCLS is represented by the RMS calculated using e_b , and the calculation formula is as follows [22].

$$RMS = \left(\sum_{b=1}^N e_b / N \right)^{0.5} \quad (4)$$

2.3.2. Extraction of Endmember Fraction

In ENVI 5.3, the minimum noise fraction rotation (MNF) was used to calculate the band eigenvalues to select the main bands by reducing the data dimensions (Figure 3a). Next, the pure pixel index was applied to identify and extract pure pixels in the multispectral data. The filtered pure pixels were used as the region of interest of the first four bands of the MNF image to generate a 3D scatter plot in the ENVI n-D visualizer. The scatter plot was rotated, and the clustered scatter clouds (endmembers) were marked (Figure 3b). Finally, the classified endmembers (Figure 3c) were substituted into FCLS to extract the component fractions.

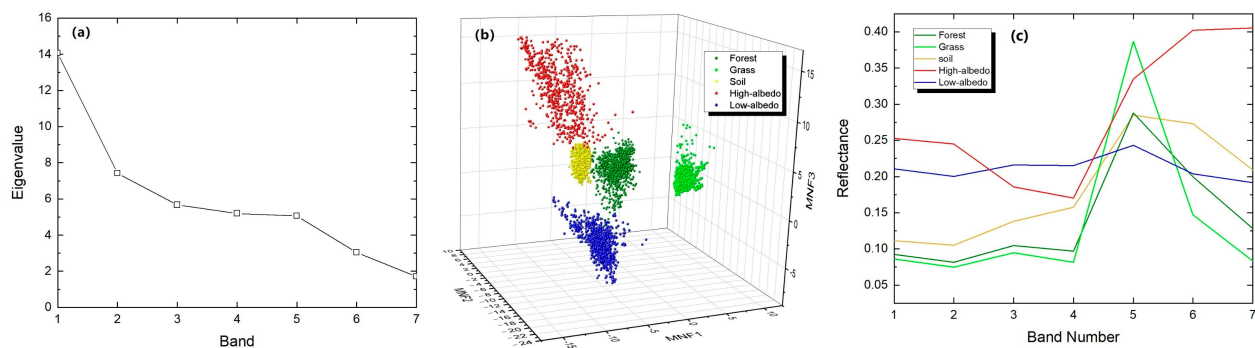


Figure 3. Endmember selection (data of 28 April 2020). (a) Eigenvalues of all minimum noise fraction rotation (MNF) bands; (b) 3D scatter plot of each endmember in MNF bands 1–3; and (c) response curve of all endmembers at each wavelength.

2.3.3. Validation of Endmember Fraction

A total of 101 sample points were generated in the study area (Figure 2c), and 101 validation sample areas of $90 \times 90 \text{ m}^2$ (3×3 pixels) were established with each sample point as the center. All sample areas were superimposed onto the mixed pixel decomposition image and GF1 image of 2020 to extract the endmember fraction inversion value and high-resolution interpretation value (true value) of each sample area. The endmembers of vegetation (forest and grassland) and IPS (high- and low-albedo) exhibited high correlation coefficients ($r > 0.89$) and linear goodness of fit ($R^2 > 0.80$) between the endmember fraction inversion value and the true value (Figure 4), indicating that the FCLS result had a high accuracy. As the four Landsat 8 images are all from May and the principles of endmember selection are completely consistent, it can be considered that the FCLS results of the four-phase data can meet the accuracy requirements.

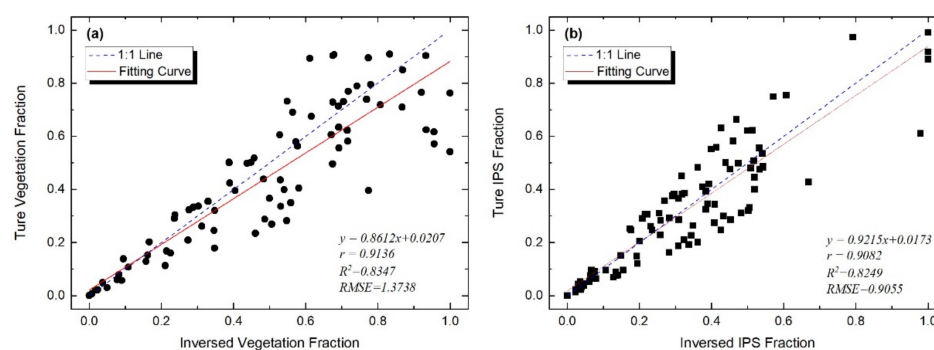


Figure 4. Validation of endmember fraction inversion results. (a) Accuracy of inverted vegetation fraction; (b) accuracy of inverted impervious surface fraction.

2.4. Analysis of Vegetation Fraction Levels Using Landscape Metrics

2.4.1. Definitions of Vegetation Fraction Levels

The mean-deviation method (Table 3) was used to classify the VFs into five levels: extreme-high VF (Level 5), sub-high VF (Level 4), medium VF (Level 3), sub-low VF (Level 2), and extreme-low VF (Level 1), which represent patches with various vegetation densities.

Table 3. Vegetation fraction levels.

VF Levels	Interval
Extreme-high VF (Level 5, LV5)	$VF > VF_{mean} + std$
Sub-high VF (Level 4, LV4)	$VF_{mean} + 0.5std < VF \leq VF_{mean} + std$
Medium VF (Level 3, LV3)	$VF_{mean} - 0.5std < VF \leq VF_{mean} + 0.5std$
Sub-low VF (Level 2, LV2)	$VF_{mean} - std < VF \leq VF_{mean} - 0.5std$
Extreme-low VF (Level 1, LV1)	$VF < VF_{mean} - std$

2.4.2. Selection of Landscape Metrics

Landscape metrics are effective tools for quantifying the spatial characteristics of various land-cover types [3]. Class-level and landscape-level metrics were used to analyze the number and spatial distribution characteristics of VF-level patches (Table 4). Five class-level metrics—percentage of landscape (PLAND), largest patch index (LPI), landscape shape index (LSI), aggregation index (AI), and patch cohesion index (COHESION)—were selected to represent the proportion, predominance, shape complexity, aggregation, and natural connectivity of patches at each VF level. Four landscape-level metrics—the Shannon diversity index (SHDI), Shannon evenness index (SHEI), patch diversity (PD), and contagion index (CONTAG)—were selected to represent the diversity, distribution, number, and aggregation degrees of all patches within an analysis unit.

2.4.3. Scale Effect Analysis

Scale effects, including the effects of grain size (spatial resolution) and spatial extent [25], are important factors that affect the results of landscape pattern analyses [26]. Landscape structure information changes with variations in grain size, and some landscape features can only be found at a specific grain size [27]. For the data of 17 May 2020, the VF-level images were resampled from 30 to 200 m at 10 m intervals to obtain the corresponding raster images with 18 spatial resolutions, and the class-level metrics for each grain size were calculated using FRAGSTATS 4.2. As shown in Figure A1a–e in Appendix B, most inflection points in the response curves appear at a grain size of 60 m. Figure A1f in Appendix B describes the land-area information-loss index calculated using Equations (A1) and (A2) in Appendix A for each grain size, indicating that the land area accuracy loss is small when the grain size is 60 m. Therefore, 60 m was selected as the best grain size for landscape pattern analysis.

Table 4. Formulas and descriptions of landscape metrics selected in this study.

Metrics	Equation	Description	Parameter Explanation
Class level	PLAND	$\left(\sum_{j=1}^n a_{ij} / A \right) \times 100$	Porportion of the patch type a_{ij} —the area of patch ij ; A —total landscape area;
	LPI	$\left[\max(a_{ij}) / A \right] \times 100$	Porportion of the largest patch type e_{ik} —total length (m) of edge in landscape between patch types (classes) i and k ;
	LSI	$0.25 \sum_{j=1}^n e_{ik} / \sqrt{A}$	Shape complexity degree of the patch type g_{ii} —number of adjacent patches of the same landscape type i ;
	AI	$\left[\frac{g_{ii}}{\max \rightarrow g_{ii}} \right] \times 100$	Aggregation degree of the patch type p_{ij} —perimeter of patch ij in terms of number of cell surfaces;
	COHESION	$\left\{ 1 - \left[\frac{\sum_{i=1}^m \sum_{k=1}^m p_{ij} / \sum_{i=1}^m \sum_{k=1}^m (p_{ij} \times \sqrt{a_{ij}})}{\left(1 - 1 / \sqrt{Z} \right)^{-1}} \right] \right\} \times 100$	Natural connectivity degree between patches Z —total number of cells in the landscape.
Landscape level	SHDI	$-\sum_{i=1}^n [p_i \times \ln(p_i)]$	Diversity indicator of all patch types p_i —proportion of the landscape occupied by patch type (class) i ;
	SHEI	$-\sum_{i=1}^n [p_i \times \ln(p_i)] / \ln(m)$	Even distribution indicator of all patch types m —number of patch types (classes) present in the landscape, excluding the landscape border if present;
	PD	N / A	Number of patches per unit area N —number of patches in the landscape of patch type (class) i ;
	CONTAG	$\left\{ 1 + \left[\frac{\sum_{i=1}^m \sum_{k=1}^m \left(p_i \times \frac{g_{ik}}{\sum_{j=1}^n g_{ij}} \right)}{\ln \left(p_i \times g_{ik} / \sum_{j=1}^n g_{ij} \right)} \right] / [2 \ln(m)] \right\} \times 100$	Aggregation degree of all patch types A —total landscape area.

The moving-window method [28,29] was used to quantify the landscape patterns of VF-level patches. Using this method, landscape metrics within a spatial extent were assigned to the center pixel for each window movement, and finally, the mapped distributions of the landscape metrics were generated. Owing to the scale dependence of the landscape metrics [30], the size of the moving window used in the calculation may affect the results [28]. When the spatial extent is smaller, the landscape index changes significantly and fluctuates greatly and hence cannot effectively reflect the gradient characteristics of the landscape patterns. When the spatial extent is larger, the landscape metrics change gently, eliminating the interference caused by high-resolution and regional differences but also leading to the loss of some gradient features. Six window sizes ranging from 300×300 to 1500×1500 m were tested at 240 m intervals. To avoid pixel splitting, the interval for the moving-window sizes was set to multiples of 60 m (the best grain size). Four landscape-level metrics were calculated for each tested window size, and then all metrics were extracted for the 101 sample points (Figure 2c) to record the metric changes under different moving-window sizes. Figure A2 shows that the curve of variation in landscape metrics tends to be stable when the spatial extent reaches 780 m. Therefore, 780 m was selected as the best spatial extent.

2.5. Landscape Surface Temperature Inversion

Landsat 8 has two thermal infrared bands: 10 and 11. However, owing to the uncertainty of band 11 information, the USGS recommends using single-channel algorithms based on band 10 for LST inversion [31,32]. The improved mono-window model [33] was used to determine the inversion parameters for the Landsat 8 sensor, as shown in Equations (5)–(7).

$$LST = \{a(1 - C - D) + [b(1 - C - D) + C + D]T_{10} - DT_{air_e}\} / C \quad (5)$$

$$C = \varepsilon\tau \quad (6)$$

$$D = (1 - \tau)[1 + (1 - \varepsilon)\tau] \quad (7)$$

where $a = -62.7182$ and $b = 0.4339$ are the linear regression coefficients of the Planck blackbody radiation function for band 10 (0–70 °C), T_{10} is the brightness temperature calculated using band 10, T_{air_e} is the effective atmospheric average temperature, ε is the surface emissivity, and τ is the atmospheric transmissivity.

$$T_{10} = K_2 / \ln(1 + K_1 / L_{10}) \quad (8)$$

$$\varepsilon_{nature} = P_v R_v \varepsilon_v + (1 - P_v) R_s \varepsilon_s + d_\varepsilon \quad (9)$$

$$\varepsilon_{construction} = P_v R_v \varepsilon_v + (1 - P_v) R_m \varepsilon_m + d_\varepsilon \quad (10)$$

where $K_1 = 774.89$ and $K_2 = 1321.08$, are the thermal conversion constants for Landsat 8 band 10; L_{10} is the thermal spectral radiance calculated from the pixel DN value of band 10 [33]; R_v , R_s , and R_m are the radiation ratios of vegetation, bare soil, and construction land, respectively [34]; $\varepsilon_v = 0.986$, $\varepsilon_s = 0.970$, and $\varepsilon_m = 0.970$, are the emissivity of pure vegetation, bare soil, and construction land, respectively; P_v is the fractional vegetation coverage; and d_ε is the effect of the interaction between vegetation and bare soil on the surface emissivity [34].

Table 5 shows the linear relationship between the mid-latitude summer effective mean atmospheric temperature (T_{air_e}) and near-surface air temperature (T_{air}) [34]. In addition, the regression functions between atmospheric transmissivity (τ) and the atmospheric water content (w) for Landsat 8 TIR band 10 were also simulated using the Moderate Resolution Atmospheric Transmission (MODTRAN 4) program [33]. Since the atmospheric water content data of the study area was not directly obtained, according to the algorithm obtained by fitting the historical observation data of the China Meteorological Stations, water content can be estimated by the average altitude of the study area ($H_E = 40$ m), the latitude of the study area ($\varphi = 34.24^\circ$), and the relative humidity (RH), which have been shown as Equations (11) and (12) [35].

$$w = 0.03 \exp(-1.39H_E^2 + 2.74H_E + 0.15)e + \frac{0.066}{(\varphi - 33)^2 + 4.41} + 0.17 \quad (11)$$

$$e = 0.6112 \exp\left(\frac{17.67T_{air}}{T_{air} + 243.5}\right) \times RH \quad (12)$$

Table 5. Regression functions for T_{air_e} and τ estimation.

w (g·cm ⁻²)	τ Functions	T_{air_e} Function
0.2–1.6	0.9184–0.0725 w	16.0110 + 0.9262 T_{air}
1.6–4.4	1.0163–0.1330 w	
4.4–5.4	0.7029–0.0620 w	

2.6. Spatial Correlation Analysis

Spatial autocorrelation analysis was used to determine whether the distribution of spatial variables was related to the adjacent variables. It can be divided into global and local spatial autocorrelations. Bivariate Moran's I [36], proposed by Anselin, can effectively reflect the correlation and dependence characteristics of the spatial distribution of two variables. OpenGeoDa software was used for bivariate spatial autocorrelation analysis. Bivariate global Moran's I was used to analyze the spatial response of LST to landscape metrics of VF-level patches; it was calculated using Equation (13).

$$I = \frac{\sum_{i=1}^n \sum_{j=1}^n W_{ij} (x_i - \bar{x})(y_j - \bar{y})}{S^2 \sum_{i=1}^n \sum_{j=1}^n W_{ij}} \quad (13)$$

where I is the bivariate global spatial autocorrelation index, that is, the overall correlation between the spatial distribution of variables x and y ; N is the total number of spatial units; W_{ij} is the spatial weight matrix established by the K adjacency method; x_i and y_j are the observed values of the independent and dependent variables in spatial units i and j , respectively; and S^2 is the variance of all samples.

Bivariate local Moran's I was calculated as follows [37]:

$$I_i = Z_i \sum_{j=1}^n W_{ij} Z_j \quad (14)$$

where I_i is the local spatial relationship between the independent and dependent variables of spatial unit i , and z_i and z_j are the standardized variance values of the observed values of spatial units i and j . Based on I_i , there are four clustering modes in the Local Indications of Spatial Association (LISA) distribution map, which can intuitively present the agglomeration and differentiation characteristics of independent and dependent variables in local areas. The clustering mode can be classified as high–high (HH) clustering, that is, the independent variable of the spatial unit i and the dependent variable of the adjacent unit j are both high; low–low (LL) clustering, that is, the independent variable of the spatial unit i and the dependent variable values of the adjacent unit j are both low; low–high (LH) aggregation, that is, the independent variable value of spatial unit i is low and the dependent variable value of the adjacent unit j is high; and high–low (HL) aggregation, that is, the independent variable value of the spatial unit i is high and the dependent variable value of the adjacent unit j is low.

2.7. Impact Weight Calculation Based on Principal Component Analysis

To further explore the contribution of the class-level metrics negatively correlated with LST in urban thermal environment mitigation, the impact weight of each metric was calculated by combining the principal component analysis (PCA) and multiple linear regression. The standardized coefficients in multiple linear regression are often used to represent the influence weight of independent variables on dependent variables. However, to prevent multicollinearity between class-level VFLMs, the multiple linear regression method cannot be used directly. In this study, PCA was used to extract the principal component variable F_i [38] for the class-level VFLMs, and standardized regression coefficients (β_i) were extracted by multiple linear regression between F_i and LST. This procedure removes the multicollinearity among the metrics, and the weighted impact (W_j) of each VFLM on LST can be obtained using the eigenvalues (λ_i), PCA component matrix (θ_{ij}), and β_i . The equations for impact weight calculation are shown as follows.

$$\alpha_{ij} = \frac{\theta_{ij}}{\sqrt{\lambda_i}} \quad (15)$$

$$F_i = \sum_{j=1}^n \alpha_{ij} X_j \quad (16)$$

$$W_j = |\alpha_{1j} \times \beta_1 + \alpha_{2j} \times \beta_2| \quad (17)$$

where X_j is the original variable; n is the total number of the original variables; α_{ij} is the contribution coefficient of original e variable in corresponding principal component variable F_i .

3. Results

3.1. Inversion Results for VF and LST

Figure 5 shows the VF maps of the study area from 2014 to 2020, which indicate the spatial distribution and area ratio of the vegetation patches. LSMA could not only extract large-area and high-proportion vegetation patches in the study area but also fully extract the fragmented and low-proportion vegetation distributions in mixed pixels, such

as small green belts near buildings and roads. Complete vegetation quantity information is beneficial for accurately exploring the effects of patches with different VFs on the thermal environment. Figure 6 shows the LST maps of the study area from 2014 to 2020, revealing that the LST values of the areas primarily covered by urban IPS were significantly higher than those of the area covered by vegetation. The superposition of the LST and VF maps indicates that the LST of patches with different VFs varies greatly. The VF and LST values of 101 sample points (Figure 2c) were extracted for correlation and linear regression analyses, as shown in Figure A3 of Appendix B. The Pearson correlation coefficients between VF and LST for the four phases were -0.6923 , -0.6226 , -0.6820 , and -0.6573 , indicating a strong negative correlation between them. The linear regression results also showed that there was a significant negative linear correlation between VF and LST ($p < 0.001$) and that for every 0.1 increase in VF, LST decreased by approximately $0.48\text{--}0.78\text{ }^{\circ}\text{C}$. Therefore, a high VF exerts a significant alleviating effect on LST, and it is necessary to further explore the spatial impact of patches with various vegetation densities on the urban thermal environment.

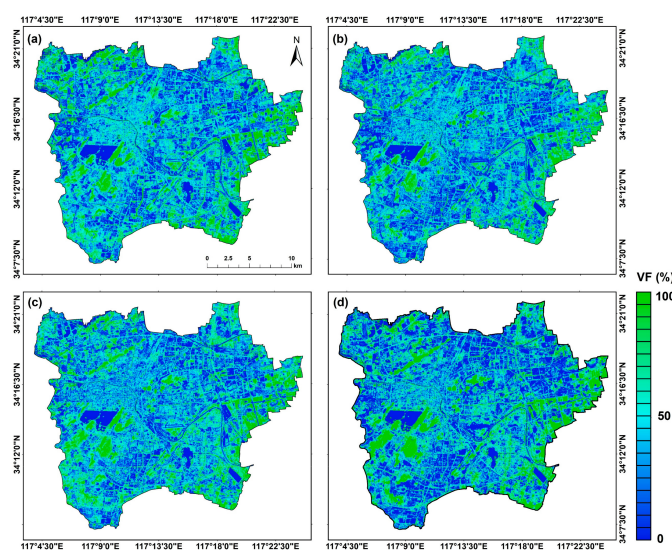


Figure 5. Vegetation fraction inversion maps of (a) 1 May 2014, (b) 16 May 2017, (c) 3 May 2018, and (d) 17 May 2020.

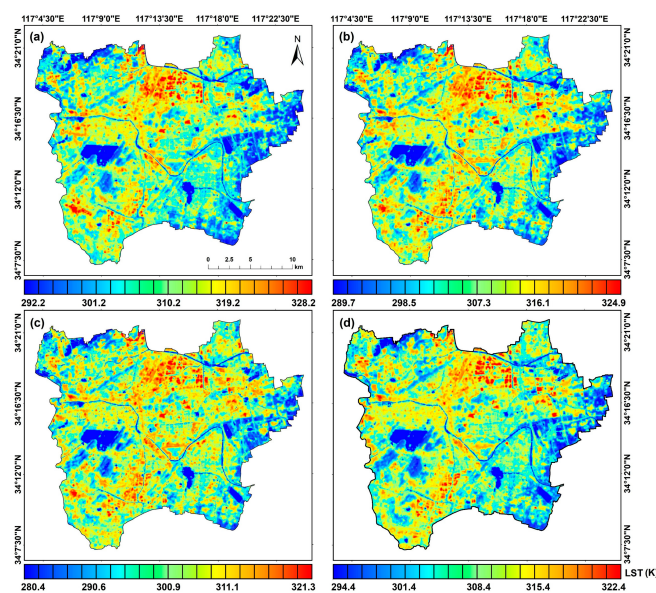


Figure 6. Land surface temperature inversion maps of (a) 1 May 2014, (b) 16 May 2017, (c) 3 May 2018, and (d) 17 May 2020.

3.2. Bivariate Moran's I between Landscape Metrics of VF-Level Patches and LST

Figure 7 shows the bivariate global Moran's I between the landscape metrics of VF-level patches (hereinafter referred to as VFLM) and LST. The spatial correlations of VFLM and LST varied widely for different landscape metrics. For the same landscape metric, the spatial correlation between VFLM and LST also varied greatly from VF LV1 to LV5. The landscape-level metrics of SHDI and PD exhibited significant negative spatial correlations with LST (average Moran's I was -0.17 and -0.13 , respectively), indicating that the region contained more types of VF levels and that patch numbers have weak effects on regional cooling. Both positive and negative spatial correlations were observed between LST and SHEI, and CONTAG, indicating that the even distribution degree and aggregation degree of the five types of VF levels have no stable influence on regional temperature. Therefore, the impact of landscape-level VFLM on LST is limited.

Class-level VFLMs such as PLAND, LPI, LSI, AI, and COHESION showed a significant spatial correlation with LST ($p < 0.001$), implying that the spatial distribution characteristics of VF-level patches, such as patch proportion, predominance degree, shape complexity degree, aggregation degree, and natural connectivity degree, are important factors for regulating environmental temperature. In addition, the bivariate global Moran's I values between VFLM and LST were positive and gradually increased from VF LV3 to LV1. In contrast, bivariate global Moran's I values between VFLM and LST were negative and gradually increased from VF LV4 to LV5. Therefore, the patch VF can effectively alleviate ambient temperature only when it reaches sub- and extreme-high levels, and the higher the VF level, the stronger the mitigation effect.

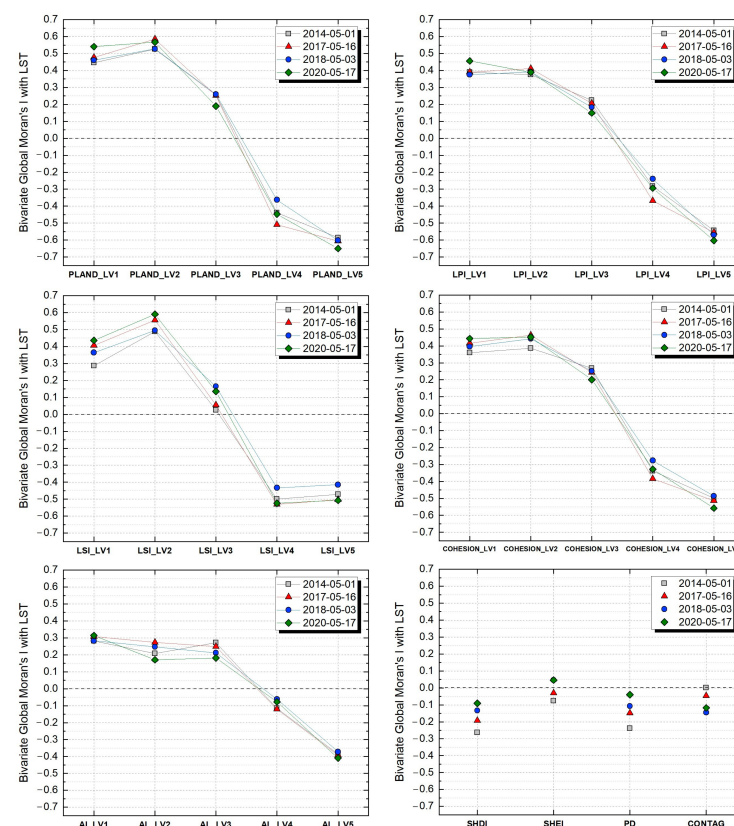


Figure 7. Bivariate global Moran's I between landscape metrics of IPSD levels and LST (the significance levels of all Moran's I were at $p < 0.001$ except for CONTAG of 1 May 2014 with $p > 0.05$).

The average values of bivariate global Moran's I between the VFLM of LV4 and LV5 patches and LST in the four phases were, from high to low, in the order of PLAND (-0.53), LPI (-0.43), LSI (-0.49), COHESION (-0.42), and AI (-0.24), indicating that patch

proportion and aggregation degree have the strongest and weakest spatial correlations with LST, respectively. However, Moran's I value cannot directly represent the contributions of these five class-level VFLMs to LST mitigation, which is necessary for further discussion of their impact.

Bivariate local Moran's I was used to further reveal the spatial characteristics of the landscape patterns of VF LV4 and LV5 patches regulating the thermal environment. The LISA maps (Figure 8) show the spatial distribution characteristics of the spatial correlation between VFLM (class level) and LST. The clustering patterns between VFLM (PLAND, LPI, LSI, AI, and COHESION) and LST were primarily HL and LH. The LH areas were primarily distributed in the urban center and mostly covered by IPS. The HL areas were primarily distributed in urban forests, parks, and suburban farmlands and were primarily covered by natural vegetation and farmland.



Figure 8. Local Indications of Spatial Association (LISA) cluster maps between landscape metrics of the vegetation fraction (VFLM; LV4 and LV5) and land surface temperature (LST): (a) 1 May 2014; (b) 16 May 2017; (c) 3 May 2018; (d) 17 May 2020 (HH: high VFLM and high LST; LL: low VFLM and low LST; LH: low VFLM and high LST; HL: high VFLM and low LST).

3.3. Impact Weight of Class-Level VFLMs of LV4 and LV5 on LST

The class-level VFLMs of LV4 and LV5 patches have been shown to have a significant negative spatial correlation with LST; however, the contribution rate of each VFLM in mitigating the thermal environment remains unclear. Therefore, it is necessary to discuss the impact weights of PLAND, LPI, LSI, COHESION, and AI of LV4 and LV5 patches in LST regulation.

The five class-level VFLMs of LV4 and LV5 patches were normalized before PCA. As listed in Table 6, the values of the Kaiser–Meyer–Olkin (KMO) measure of sampling

adequacy for the four phases were all greater than 0.6, indicating that the PCA method is feasible for analyzing these variables. Two principal components (F_1 and F_2) were extracted from each phase, with a high proportion of cumulative variance (>77%).

Table 7 lists the loadings of the original variables in the principal components (F_1 and F_2). A common feature is that the metrics of LV5 (X1–X5) and LV4 (X6–X10) are the core parameters affecting the principal components F_1 and F_2 , respectively (with high θ_i values; values with $\theta_i < 0.3$ have been rejected). Therefore, F_1 and F_2 can be used as new variables to represent the class-level VFLMs of LV5 and LV4 patches, respectively. Equation (15) was used to calculate the contribution coefficient (α_{ij}) of each original variable based on eigenvalues (λ_i) and θ_i , and F_1 and F_2 were calculated using Equation (16).

Table 6. Total variance explained from principal component analysis (PCA).

Date	KMO	Sums of Squared Loadings	F_1 [Ⓢ]	F_2 [Ⓢ]
1 May 2014	0.7190	Eigenvalue (λ_i)	4.02	3.74
		Cumulative percent (%)	77.56	
16 May 2017	0.7109	Eigenvalue (λ_i)	4.00	3.71
		Cumulative percent (%)	77.14	
3 May 2018	0.7096	Eigenvalue (λ_i)	3.89	3.84
		Cumulative percent (%)	77.32	
17 May 2020	0.6855	Eigenvalue (λ_i)	3.89	3.88
		Cumulative percent (%)	77.74	

[Ⓢ] F_1 and F_2 are components 1 and 2 extracted using PCA, respectively.

Table 7. Component matrix of principle component analysis [Ⓢ].

Normalized Original Variables (Class-Level VFLMs)	1 May 2014		16 May 2017		3 May 2018		17 May 2020	
	F_1 (θ_1)	F_2 (θ_2)	F_1 (θ_1)	F_2 (θ_1)	F_1 (θ_1)	F_2 (θ_2)	F_1 (θ_1)	F_2 (θ_2)
(X1) PLAND_LV5	0.914	/	0.910	/	0.914	/	0.921	/
(X2) COHESION_LV5	0.914	/	0.911	/	0.909	/	0.914	/
(X3) LPI_LV5	0.883	/	0.880	/	0.885	/	0.891	/
(X4) AI_LV5	0.827	/	0.838	/	0.826	/	0.823	/
(X5) LSI_LV5	0.627	0.572	0.611	0.586	0.596	/	0.579	/
(X6) PLAND_LV4	0.341	0.875	0.372	0.868	0.300	0.896	/	0.908
(X7) COHESION_LV4	/	0.923	/	0.924	/	0.924	/	0.935
(X8) LPI_LV4	/	0.873	/	0.883	/	0.880	/	0.883
(X9) AI_LV4	/	0.733	/	0.705	/	0.733	/	0.724
(X10) LSI_LV4	0.555	0.632	0.531	0.624	0.513	0.631	0.519	0.642

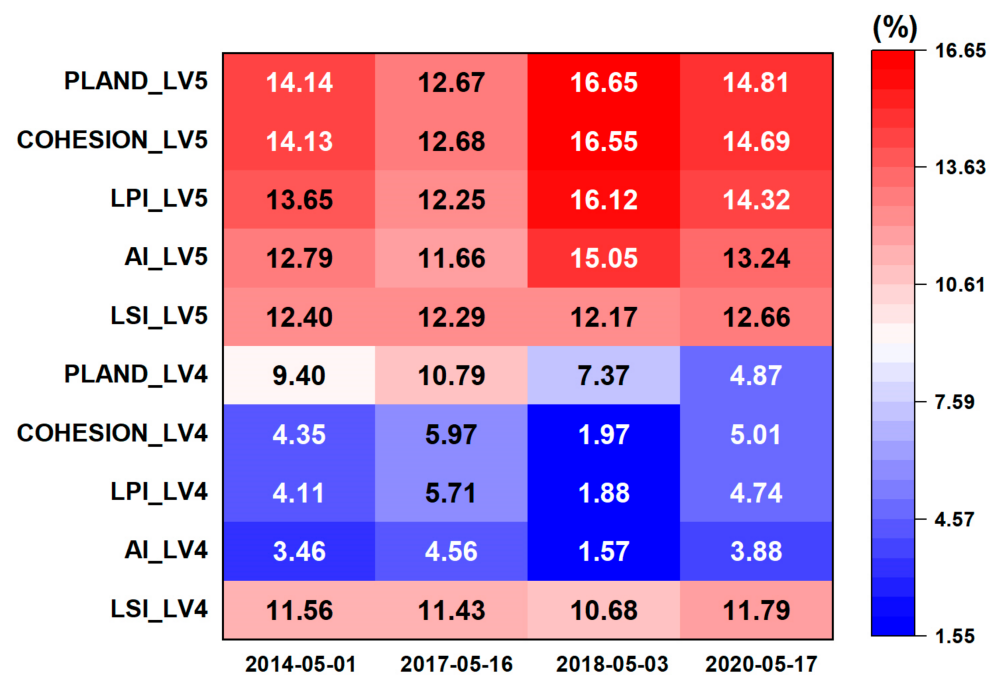
[Ⓢ] Rotation method: Varimax with Kaiser normalization.

Multiple linear regressions between normalized LST (LST_N) and F_1 and F_2 (Table 8) of the four phases showed significant negative linear correlations between them ($p < 0.001$). The absolute values of the standardized coefficients (β_1) of F_1 were all larger than those of F_2 (β_2), indicating that the class-level VFLM of LV5 had a stronger regulatory effect on LST than that of LV4. Finally, the impact weights (W_j) of all class-level VFLMs were calculated using Equation (17), and the results are shown in Figure 9.

The heat map in Figure 9 again shows that the class-level VFLM of LV5 has a higher impact weight on LST than that of LV4 and that PLAND_LV5 (X1) and COHESION_LV5 (X2) had the highest impact weights among all metrics, indicating that patch proportion and natural connectivity degree between LV5 patches are the two most important factors affecting LST, followed by LPI_LV5 (X3), AI_LV5 (X4), and LSI_LV5 (X5). In contrast to LV5, the impact weights of the class-level VFLM of LV4 were, from high to low, in the order of LSI_LV4 (X10), PLAND_LV4 (X6), COHESION_LV4 (X7), LPI_LV4 (X8), and AI_LV4 (X9). In urban areas, the land-cover type of the LV5 patch is almost entirely vegetation; however, the LV4 patch is still mixed with more land-cover types, which is the main reason for the difference in the orders of impact weights between the VFLMs of LV4 and LV5.

Table 8. Results of multiple linear regression between dependent variable LST_N and independent variables F_1 and F_2 .

Regression Coefficients		1 May 2014	16 May 2017	3 May 2018	17 May 2020
r		0.569 ***	0.612 ***	0.553 ***	0.644 ***
R^2		0.323 ***	0.375 ***	0.306 ***	0.415 ***
Regression Constant		0.949 ***	0.578 ***	0.693 ***	0.635 ***
Unstandardized Coefficients	F_1	−0.010 ***	−0.110 ***	−0.083 ***	−0.109 ***
	F_2	−0.004 ***	−0.066 ***	−0.014 ***	−0.054 ***
Standardized Coefficients (β_i)	β_1	−0.474 ***	−0.463 ***	−0.516 ***	−0.538 ***
	β_2	−0.139 ***	−0.207 ***	−0.060 ***	−0.179 ***

*** Significant: $p < 0.001$.**Figure 9.** Heatmap of the impact weights of vegetation-fraction landscape metrics on land surface temperature.

4. Discussion

In previous studies on the relationship between green space and LST based on mid- or low-resolution satellite images, vegetation was generally regarded as one or several kinds of homogeneous patches (such as grassland, farmland, and forest) in landscape pattern analysis [12,15,39], without considering the spatial impact of vegetation density on the thermal environment. Since vegetation density has been proven to have significant negative correlations with LST [40,41], an innovative method was explored to incorporate vegetation density into landscape pattern analysis in this study. According to the fraction value of vegetation component from low to high, the land surface of the study area was classified into five levels (or five patch types), which is similar to the land-cover types. A same index is used to classify the urban surface with high heterogeneity, which is conducive to revealing the difference in the impacts of the spatial patterns of patches with various vegetation densities on UHI regulation.

The results showed that there were differences in the impacts of landscape-level and class-level metrics on LST. Particularly, the effects of the landscape-level SHEI and CON-TAG on LST were unstable (both positive and negative effects exist). This is mainly because landscape-level metrics represent the regional spatial characteristics of five vegetation den-

sity levels, which includes both the mitigation effects of high-vegetation-density patches on the thermal environment and the enhancement impacts of low-vegetation-density patches (with a higher density of impervious surfaces) on the surface temperature. Therefore, the impacts of the even distribution degree and aggregation degree of the five vegetation levels on LST depend on which level is dominant in the region. This phenomenon is consistent with the previous research. On the premise that the land surfaces are divided into grassland, forest, farmland, impervious water, and other types, the correlations of LST with landscape-level metrics such as AI, LPI, CONTAG, SHDI, and PD are unstable (with variable correlation directions and significances) [3,42].

The absolute value of the spatial correlation between class-level metrics and LST ($|Moran's I|$) gradually decreases from LV1 to LV3 and conversely increases gradually from LV4 to LV5. This phenomenon is also owing to the variation in vegetation density among different patches. From LV1 to LV3, the patches' spatial patterns were positively correlated with LST, because these patches were primarily covered by IPS and because the vegetation cooling effect could not offset the heating effect caused by the IPS thermal radiation and anthropogenic heat. However, as the vegetation density gradually increased and the impervious surface density gradually decreased, resulting in a decreasing trend of $|Moran's I|$. From LV4 to LV5, the spatial pattern of patches was negatively correlated with LST, because these patches were dominated by vegetation cover and because their cooling effect was sufficient to control the ambient temperature. Furthermore, owing to the gradual increase in vegetation density, $|Moran's I|$ showed an increasing trend. In addition, the land-cover types of the LV5 patches were almost entirely vegetation. However, the LV4 patches were still mixed with more land-cover types. This is an important reason for the difference in the orders of impact weights between the VFLMs of LV4 and LV5. In previous studies, for the patches of forest, grassland, and farmland, their class-level metrics of PLAND, LSI, and AI were found to be negatively correlated with LST, and the correlation between PLAND and LST was far stronger than AI [42], which is also consistent with our results. According to our research, priority should be given to increasing the area ratio, natural connectivity, and shape complexity degrees of high-density vegetation, which can effectively enhance the ability of green space in regional UHI mitigation.

5. Conclusions

In this study, four periods of Landsat 8 OLI/TIRS images and various geospatial methods (including landscape measurement, spatial correlation, and statistics) were used to examine the spatial relationship between LST and the landscape patterns of patches with various vegetation densities. There was a certain spatial correlation between the landscape metrics of the five VF-level patches and LST. Landscape-level metrics such as SHDI and PD only have significant but weak negative spatial correlations with LST, indicating that the types of VF levels and number of patches have limited impacts on regional temperature. However, all class-level metrics, such as PLAND, COHESION, LPI, LSI, and AI, of extreme- and sub-high-level patches had significant negative spatial correlations with LST, and the correlation degree was high. This indicates that spatial distribution characteristics such as patch proportion, natural connectivity degree, predominance degree, shape complexity, and aggregation degree of areas with high vegetation density are important factors in regulating the thermal environment. In addition, patches with high VF levels have a strong ability to alleviate surface temperature; in particular, PLAND and COHESION of VF LV5 patches have the highest impact weights on LST. These findings reveal the importance of and differences in the spatial patterns of areas with various VFs in urban thermal environment regulation, thus providing new perspectives and references for urban green-space planning and climate management.

Special attention should be paid to the fact that different vegetation types have significant differences in evapotranspiration, shading, canopy heat radiation characteristics, etc., so their spatial patterns will have different impact mechanisms on LST. Further research is required on the distinction of the regulatory effects of the spatial patterns of the

vegetation types with different canopy characteristics on LST, with the help of Uninhabited Air Vehicles (UAV) or high-resolution satellites equipped with multi-spectral and thermal infrared sensors.

Author Contributions: Conceptualization, Y.Z. and Y.W.; methodology, Y.Z.; software, N.D.; validation, Y.W.; formal analysis, Y.Z.; data curation, Y.Z.; writing—original draft preparation, Y.Z.; writing—review and editing, Y.W.; visualization, N.D.; supervision, N.D.; funding acquisition, Y.Z. and N.D. All authors have read and agreed to the published version of the manuscript.

Funding: This research was funded by the National Natural Science Foundation of China, Grant Nos. 42101256 and 41904013, and is a project funded by the Priority Academic Program Development of Jiangsu Higher Education Institutions (PAPD) (The Fourth Phase).

Data Availability Statement: Not applicable.

Acknowledgments: The authors would like to thank the United States Geological Survey for supporting Landsat 8 data. Further, we thank China University of Mining and Technology and the NOAA National Centers for Environmental Information of USA for providing meteorological data. The comments and suggestions of the editor and the anonymous reviewers are gratefully acknowledged.

Conflicts of Interest: The authors declare no conflict of interest.

Appendix A

$$L_j = (A_j - A_{bj}) / A_{bj} \times 100 \quad (A1)$$

$$S_j = \sqrt{\frac{\sum_{j=1}^n L_j^2}{n}} \quad (A2)$$

where L_j refers to the relative value of area loss; A_j is the area of VF level j at a converted grain size; A_{bj} is the area of VF level j at the original grain size; n is the number of VF levels, and S_j is the land area loss index.

Appendix B

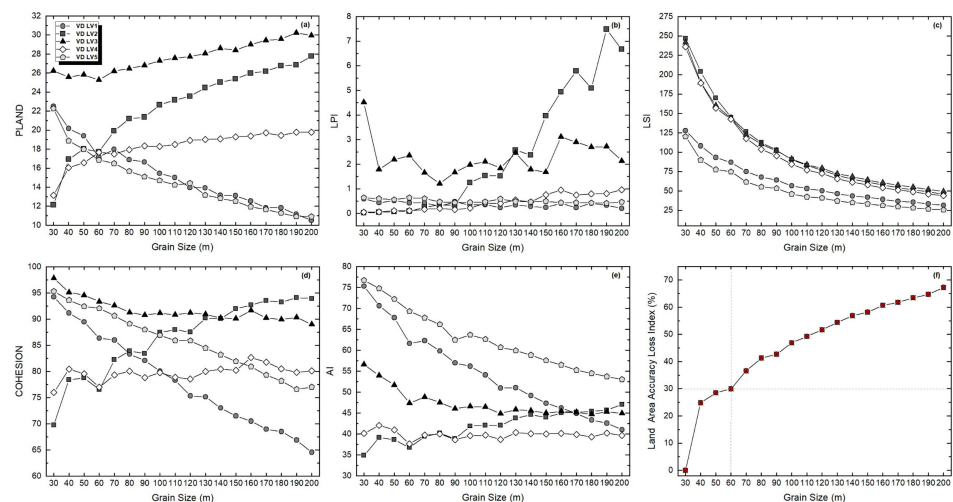


Figure A1. (a–e) Response curves of class–level metrics against variations in grain size; (f) land area loss index curve corresponding to grain size variation.

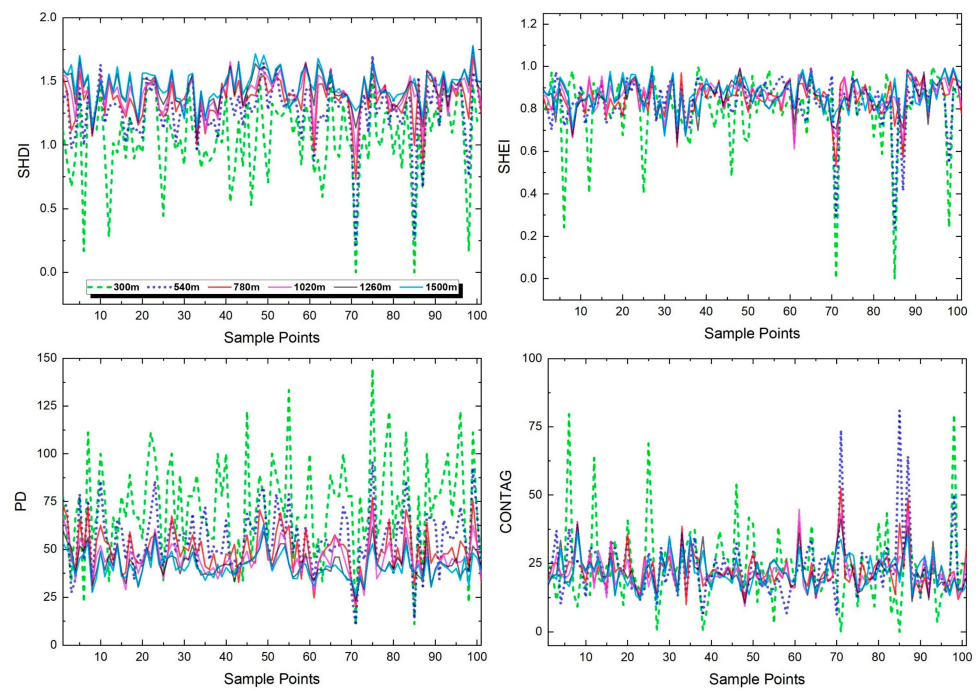


Figure A2. Trends in the variation of landscape-level metrics of 101 sample points for different spatial extents.

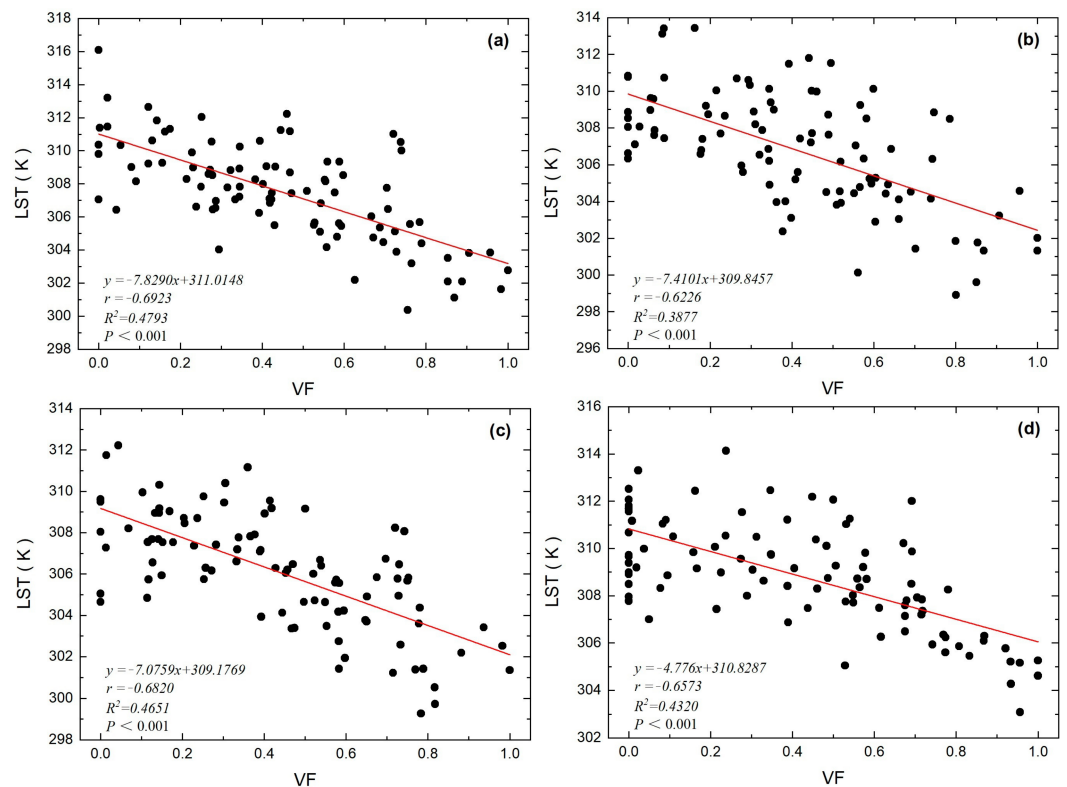


Figure A3. Linear regression between vegetation fraction and land surface temperature of sample points: (a) 1 May 2014; (b) 16 May 2017; (c) 3 May 2018; and (d) 17 May 2020.

References

1. He, B.-J.; Wang, J.; Zhu, J.; Qi, J. Beating the Urban Heat: Situation, Background, Impacts and the Way Forward in China. *Renew. Sustain. Energy Rev.* **2022**, *161*, 112350. [[CrossRef](#)]
2. Santamouris, M. Recent Progress on Urban Overheating and Heat Island Research. Integrated Assessment of the Energy, Environmental, Vulnerability and Health Impact. Synergies with the Global Climate Change. *Energy Build.* **2020**, *207*, 109482. [[CrossRef](#)]
3. Rakoto, P.Y.; Deilami, K.; Hurley, J.; Amati, M.; Sun, Q. (Chayn) Revisiting the Cooling Effects of Urban Greening: Planning Implications of Vegetation Types and Spatial Configuration. *Urban For. Urban Green.* **2021**, *64*, 127266. [[CrossRef](#)]
4. Amati, M.; Taylor, L. From Green Belts to Green Infrastructure. *Plan. Pract. Res.* **2010**, *25*, 143–155. [[CrossRef](#)]
5. Chen, A.; Yao, X.A.; Sun, R.; Chen, L. Effect of Urban Green Patterns on Surface Urban Cool Islands and Its Seasonal Variations. *Urban For. Urban Green.* **2014**, *13*, 646–654. [[CrossRef](#)]
6. Shih, W. Greenspace Patterns and the Mitigation of Land Surface Temperature in Taipei Metropolis. *Habitat Int.* **2017**, *60*, 69–80. [[CrossRef](#)]
7. Bowler, D.E.; Buyung-Ali, L.; Knight, T.M.; Pullin, A.S. Urban Greening to Cool Towns and Cities: A Systematic Review of the Empirical Evidence. *Landsc. Urban Plan.* **2010**, *97*, 147–155. [[CrossRef](#)]
8. Horváthová, E.; Badura, T.; Duchková, H. The Value of the Shading Function of Urban Trees: A Replacement Cost Approach. *Urban For. Urban Green.* **2021**, *62*, 127166. [[CrossRef](#)]
9. Colter, K.R.; Middel, A.C.; Martin, C.A. Effects of Natural and Artificial Shade on Human Thermal Comfort in Residential Neighborhood Parks of Phoenix, Arizona, USA. *Urban For. Urban Green.* **2019**, *44*, 126429. [[CrossRef](#)]
10. Deilami, K.; Rudner, J.; Butt, A.; MacLeod, T.; Williams, G.; Romeijn, H.; Amati, M. Allowing Users to Benefit from Tree Shading: Using a Smartphone App to Allow Adaptive Route Planning during Extreme Heat. *Forests* **2020**, *11*, 998. [[CrossRef](#)]
11. Hsieh, C.M.; Li, J.J.; Zhang, L.; Schwegler, B. Effects of Tree Shading and Transpiration on Building Cooling Energy Use. *Energy Build.* **2018**, *159*, 382–397. [[CrossRef](#)]
12. Wang, X.; Dallimer, M.; Scott, C.E.; Shi, W.; Gao, J. Tree Species Richness and Diversity Predicts the Magnitude of Urban Heat Island Mitigation Effects of Greenspaces. *Sci. Total Environ.* **2021**, *770*, 145211. [[CrossRef](#)] [[PubMed](#)]
13. Lee, P.S.-H.; Park, J. An Effect of Urban Forest on Urban Thermal Environment in Seoul, South Korea, Based on Landsat Imagery Analysis. *Forests* **2020**, *11*, 630. [[CrossRef](#)]
14. Zhang, Y.; Chen, L.L.; Wang, Y.; Chen, L.L.; Yao, F.; Wu, P.; Wang, B.; Li, Y.; Zhou, T.; Zhang, T. Research on the Contribution of Urban Land Surface Moisture to the Alleviation Effect of Urban Land Surface Heat Based on Landsat 8 Data. *Remote Sens.* **2015**, *7*, 10737–10762. [[CrossRef](#)]
15. Guo, G.; Wu, Z.; Chen, Y. Complex Mechanisms Linking Land Surface Temperature to Greenspace Spatial Patterns: Evidence from Four Southeastern Chinese Cities. *Sci. Total Environ.* **2019**, *674*, 77–87. [[CrossRef](#)]
16. Estoque, R.C.; Murayama, Y.; Myint, S.W. Effects of Landscape Composition and Pattern on Land Surface Temperature: An Urban Heat Island Study in the Megacities of Southeast Asia. *Sci. Total Environ.* **2017**, *577*, 349–359. [[CrossRef](#)]
17. Zhou, W.; Cao, F. Effects of Changing Spatial Extent on the Relationship between Urban Forest Patterns and Land Surface Temperature. *Ecol. Indic.* **2020**, *109*, 105778. [[CrossRef](#)]
18. NOAA's Satellite and Information Service (NESDIS) NOAA National Centers for Environmental Information. Available online: <https://www.ngdc.noaa.gov/> (accessed on 7 September 2022).
19. Li, L.; Canters, F.; Solana, C.; Ma, W.; Chen, L.; Kervyn, M. Discriminating Lava Flows of Different Age within Nyamuragira's Volcanic Field Using Spectral Mixture Analysis. *Int. J. Appl. Earth Obs. Geoinf.* **2015**, *40*, 1–10. [[CrossRef](#)]
20. Heinz, D.C.D.C.; Chang, C.I. Fully Constrained Least Squares Linear Spectral Mixture Analysis Method for Material Quantification in Hyperspectral Imagery. *IEEE Trans. Geosci. Remote Sens.* **2001**, *39*, 529–545. [[CrossRef](#)]
21. Small, C. Estimation of Urban Vegetation Abundance by Spectral Mixture Analysis. *Int. J. Remote Sens.* **2001**, *22*, 1305–1334. [[CrossRef](#)]
22. Wu, C.; Murray, A.T. Estimating Impervious Surface Distribution by Spectral Mixture Analysis. *Remote Sens. Environ.* **2003**, *84*, 493–505. [[CrossRef](#)]
23. Ridd, M.K. Exploring a V-I-S (Vegetation-Impervious Surface-Soil) Model for Urban Ecosystem Analysis through Remote Sensing: Comparative Anatomy for Cities. *Int. J. Remote Sens.* **1995**, *16*, 2165–2185. [[CrossRef](#)]
24. Wu, C. Normalized Spectral Mixture Analysis for Monitoring Urban Composition Using ETM+ Imagery. *Remote Sens. Environ.* **2004**, *93*, 480–492. [[CrossRef](#)]
25. Wu, J. Effects of Changing Scale on Landscape Pattern Analysis: Scaling Relations. *Landsc. Ecol.* **2004**, *19*, 125–138. [[CrossRef](#)]
26. Teng, M.; Zeng, L.; Zhou, Z.; Wang, P.; Xiao, W.; Dian, Y. Responses of Landscape Metrics to Altering Grain Size in the Three Gorges Reservoir Landscape in China. *Environ. Earth Sci.* **2016**, *75*, 1055. [[CrossRef](#)]
27. Oyana, T.J.; Johnson, S.J.; Wang, G. Landscape Metrics and Change Analysis of a National Wildlife Refuge at Different Spatial Resolutions. *Int. J. Remote Sens.* **2014**, *35*, 3109–3134. [[CrossRef](#)]
28. Chefaoui, R.M. Landscape Metrics as Indicators of Coastal Morphology: A Multi-Scale Approach. *Ecol. Indic.* **2014**, *45*, 139–147. [[CrossRef](#)]
29. Kong, F.; Nakagoshi, N. Spatial-Temporal Gradient Analysis of Urban Green Spaces in Jinan, China. *Landsc. Urban Plan.* **2006**, *78*, 147–164. [[CrossRef](#)]

30. Wu, J.; Shen, W.; Sun, W.; Tueller, P.T. Empirical Patterns of the Effects of Changing Scale on Landscape Metrics. *Landscape Ecol.* **2002**, *17*, 761–782. [[CrossRef](#)]
31. Barsi, J.; Schott, J.; Hook, S.; Raqueno, N.; Markham, B.; Radocinski, R. Landsat-8 Thermal Infrared Sensor (TIRS) Vicarious Radiometric Calibration. *Remote Sens.* **2014**, *6*, 11607–11626. [[CrossRef](#)]
32. Montanaro, M.; Lunsford, A.; Tesfaye, Z.; Wenny, B.; Reuter, D. Radiometric Calibration Methodology of the Landsat 8 Thermal Infrared Sensor. *Remote Sens.* **2014**, *6*, 8803–8821. [[CrossRef](#)]
33. Wang, F.; Qin, Z.; Song, C.; Tu, L.; Karnieli, A.; Zhao, S. An Improved Mono-Window Algorithm for Land Surface Temperature Retrieval from Landsat 8 Thermal Infrared Sensor Data. *Remote Sens.* **2015**, *7*, 4268–4289. [[CrossRef](#)]
34. Qin, Z.; Karnieli, A.; Berliner, P. A Mono-Window Algorithm for Retrieving Land Surface Temperature from Landsat TM Data and Its Application to the Israel-Egypt Border Region. *Int. J. Remote Sens.* **2001**, *22*, 3719–3746. [[CrossRef](#)]
35. Zhang, Y.; Li, L.; Chen, L.; Liao, Z.; Wang, Y.; Wang, B.; Yang, X. A Modified Multi-Source Parallel Model for Estimating Urban Surface Evapotranspiration Based on ASTER Thermal Infrared Data. *Remote Sens.* **2017**, *9*, 1029. [[CrossRef](#)]
36. Anselin, L. Local Indicators of Spatial Association—LISA. *Geogr. Anal.* **1995**, *27*, 93–115. [[CrossRef](#)]
37. Zhang, Y.; Liu, Y.; Zhang, Y.; Liu, Y.; Zhang, G.; Chen, Y. On the Spatial Relationship between Ecosystem Services and Urbanization: A Case Study in Wuhan, China. *Sci. Total Environ.* **2018**, *637–638*, 780–790. [[CrossRef](#)]
38. Liu, R.X.; Kuang, J.; Gong, Q.; Hou, X.L. Principal Component Regression Analysis with Spss. *Comput. Methods Programs Biomed.* **2003**, *71*, 141–147. [[CrossRef](#)]
39. Dutta, K.; Basu, D.; Agrawal, S. Synergetic Interaction between Spatial Land Cover Dynamics and Expanding Urban Heat Islands. *Environ. Monit. Assess.* **2021**, *193*, 184. [[CrossRef](#)]
40. Wetherley, E.B.; McFadden, J.P.; Roberts, D.A. Megacity-Scale Analysis of Urban Vegetation Temperatures. *Remote Sens. Environ.* **2018**, *213*, 18–33. [[CrossRef](#)]
41. Zaitunah, A.; Samsuri, S.; Silitonga, A.F.; Syaufina, L. Urban Greening Effect on Land Surface Temperature. *Sensors* **2022**, *22*, 4168. [[CrossRef](#)]
42. Zhao, H.; Tan, J.; Ren, Z.; Wang, Z. Spatiotemporal Characteristics of Urban Surface Temperature and Its Relationship with Landscape Metrics and Vegetation Cover in Rapid Urbanization Region. *Complexity* **2020**, *2020*, 1–12. [[CrossRef](#)]